



Machine learning driven chemiluminescence-based modelling of combustion parameters in premixed swirling NH₃/H₂ flames

Nwode Agwu^{*} , Jordan Davies, Daisuke Sato , Syed Mashruk , Agustin Valera-Medina 

College of Physical Sciences and Engineering, Cardiff University, CF24 3AA, Wales, UK

ARTICLE INFO

Handling Editor: Dr M Djukic

Keywords:

Equivalence ratio
Ammonia fraction
Explicit
NOx emissions
Bayesian regularisation

ABSTRACT

This work develops predictive models for estimating equivalence ratio (ϕ), ammonia fraction ($x\text{NH}_3$) and noxious emissions (NOx) from the flames of turbulent premixed NH₃/H₂ fuel blend stabilised using a tangential swirl burner. Bayesian Regularisation Artificial Neural Network (BR-ANN) is utilized to estimate both ϕ and $x\text{NH}_3$ with excited ratios NH^{*}/OH^{*}, violet/OH^{*} and NH₂^{*}/NO₂^{*} as inputs. NOx was predicted with NO^{*}, OH^{*}, NH^{*}, NH₂^{*} and NO₂^{*} as input variables. The coefficient of determination (R^2) was 0.98, 0.95, 0.99, 0.99 and 0.97 for the ϕ , $x\text{NH}_3$, NO, NO₂ and N₂O models, respectively. The models show better performance when compared to the conventional ratio-based method of inferring crucial combustion features. The developed models operate within the ranges of ammonia-hydrogen blend ($0.55 \leq x\text{NH}_3 \leq 0.90$), Reynolds numbers ($4000 \leq \text{Re} \leq 7000$), equivalence ratios ($0.60 \leq \phi \leq 1.40$), room temperature and atmospheric pressure. The models have been explicitly presented in mathematical equations enabling easy deployment in a software. These models will serve as a crucial step towards the development of non-invasive sensors that will help designers easily determine location of interest, predict reaction zones formation according to ϕ and $x\text{NH}_3$ and advance approaches that abate NOx emissions.

1. Introduction

Ammonia (NH₃) is a carbon-free fuel with high energy density and an established global transport infrastructure, making it a promising candidate for clean energy applications. However, ammonia-only combustion faces significant challenges due to its low flame speed, high ignition temperature, and tendency to form harmful nitrogen oxides (NOx). These issues make stable combustion and emissions control difficult in engines and turbines. To address this, researchers are exploring fuel blending strategies, particularly with hydrogen (H₂). Hydrogen is a clean, reactive fuel that enhances ammonia's combustion properties but suffers from storage and distribution limitations. Blending hydrogen with ammonia significantly improves flame stability, reduces ignition delay, and lowers unburned ammonia emissions. This combination allows for more efficient and cleaner combustion, making it a strong candidate for low-emission energy systems. Ongoing research focuses on optimizing blend ratios and combustion conditions to support the transition to a carbon-neutral energy future. [1,2]. Several companies have keyed into the potentials of ammonia and hydrogen as energy source to reduce carbon footprint worldwide. Mitsubishi Power had

a successful demonstration of a fuel mixture with 30 % hydrogen in a J-series Air-Cooled (JAC) gas turbine. This is after they had completed tests on an NH₃ single-fuel burner used for firing of coal by their parent company [3]. The likes of Doosan, KEPSCO, and Samsung are also collaborating to develop a dual-fuel green NH₃ power generation model that aims to deploy a 1 GW power plant in South Korea [4]. Amogy has retrofitted a tugboat to operate on cleanly-made ammonia, demonstrating the potential of ammonia as a carbon-free fuel in maritime applications. The system splits ammonia into hydrogen and nitrogen to power an electric fuel cell helping in achieving zero carbon emissions [5].

The analysis of NOx emissions helps in the monitoring and optimisation of practical burner systems with flame supervision offering an efficient and safe method for achieving this. Ballester and Garcia-Armigol [6] noted that monitoring of practical combustion equipment can be done in several ways including using pressure transducers, probing, imaging techniques and optical sensors. The analysis of light released from excited species such as OH^{*}, NH^{*}, NH₂^{*} etc. after their production from chemical reactions during combustion is vital in combustion technology [7]. Recently, laser absorption spectroscopy has emerged as a highly promising method for the diagnosis of flames. The

^{*} Corresponding author.

E-mail address: agwune@cardiff.ac.uk (N. Agwu).

<https://doi.org/10.1016/j.ijhydene.2025.06.062>

Received 18 January 2025; Received in revised form 18 April 2025; Accepted 3 June 2025

Available online 11 June 2025

0360-3199/© 2025 The Authors. Published by Elsevier Ltd on behalf of Hydrogen Energy Publications LLC. This is an open access article under the CC BY license (<http://creativecommons.org/licenses/by/4.0/>).

Abbreviations			
a	strain rate	j	Index representing the number of inputs
AFT	Adiabatic Flame Temperature	LW	Hidden-Output layer weights
AAPE	Average Absolute Percent Error	ML	Machine Learning
ANN	Artificial Neural network	MSE	Mean Square Error
b1	Bias applied between input and hidden layers	NN	Neural Network
b2	Bias applied hidden and output layers	R^2	Coefficient of determination
BR	Bayesian Regularisation	Re	Reynolds number
FLIPS	Femtosecond Laser-Induced Plasma Spectroscopy	RMSE	Root Mean Square Error
GPR	Gaussian Process Regression	xNH_3	Ammonia fraction
i	Index representing the number of neurons	xNH_{3n}	Normalised value of ammonia fraction
IW	Input-Hidden layer weights	ϕ	Equivalence ratio
		ϕ_n	Normalised value of equivalence ratio

reactions involving excited radicals are strongly correlated with temperature as well as contain oxidizing species and these combination makes the chemiluminescence emissions produced to be intricately linked to the flame properties. Due to its cost efficient and less complicated setup, chemiluminescence based diagnostics have been employed severally in the laboratory and industry to measure key combustion parameters [8,9] thus serving as a highly sensitive and non-invasive method for monitoring and optimisation. Precisely controlling equivalence ratios in fuel blends can help avoid blowoffs in gas turbines, pressure waves induced flashbacks and combustor damage owing to oscillations when turbines operate close to the limit of lean combustion [10,11].

Few studies have been conducted on ammonia flames due to its low combustion features. However, research on the spectrum of ammonia related flames have been carried out even as far back as 1931 when Fowler et al. [12] observed that hydrogen nitrous oxide flame in the spectral range of $\lambda 8225$ to $\lambda 2250$ is identical to the flame of ammonia/oxygen combustion with the exception of certain bands in the spectra owing to varying intensities. Later on Wolfhard et al. [13] explored ammonia-oxygen and ethylene-oxygen flames spectroscopically using a flat flame technique. They quantitatively measured the molecular oxygen and OH radical concentrations with results showing that at atmospheric pressure, diffusion flames with oxygen have a similar structure as that of a flame whose rate is established by diffusion.

Using a nozzle-type burner, Hayakawa et al. [14] analysing the chemiluminescence of premixed NH_3 /air flames at various ϕ and pressures noted that the orange colour of the NH_3 flame is influenced by H_2O vapour spectra and the NH_2 ammonia α band. NO production is restricted by H and OH radical consumption through the reaction $OH + H + M \rightleftharpoons H_2O + M$. Zhang et al. [15] utilising femtosecond laser-induced plasma spectroscopy (FLIPS), measured the chemiluminescence spectra of premixed NH_3 /air flames and concluded that the ratio NH (336 nm)/ N_2 (337 nm) could sense ϕ .

To improve the combustion intensity of ammonia and reduce noxious emissions simultaneously, Valera-Medina et al. [16] investigated numerically and experimentally the combustion of a lean premixed 50 % NH_3 /50 % H_2 blend in a generic swirl combustor. They found that the mixture produced laminar flame speeds like methane and a potential for flashback caused by the high diffusivity of hydrogen. O and OH radicals identified in the study caused high NOx emissions. Stratification with hydrogen injection in low swirl combustors was recommended to deal with the instabilities. Pugh et al. [48] using a combination of OH^* , NH_2^* and NH^* chemiluminescence with ammonia flames and 70 % NH_3 /30 % H_2 flames as a function of their inlet gas temperature observed that in rich NH_3 flames, NH_2^* intensity serves as a good indicator for NO consumption.

In a recent study, Zhu et al. [17] explored this zero carbon blend and analysed its UV–visible chemiluminescence using a counterflow burner for expansive ranges of ammonia fractions ($0.55 \leq xNH_3 \leq 0.90$), strain

rates ($50 \leq a \leq 300/s$) and equivalence ratios ($0.35 \leq \phi \leq 1.70$). They found that ratios $OH^*/violet$ and OH^*/NO^* are good indicators for ϕ for lean and rich NH_3/H_2 flames, respectively, insensitive to xNH_3 and slightly sensitive to strain rate. Ratio red/blue served as a good surrogate for xNH_3 , but it is globally insensitive to strain rate. Based on the experimental data from the study, Konnov [18] developed a model that describes the production and consumption of radicals such as NH_2^* , NO_2^* , NH^* and $NO(A)$. He found good agreements with the experimental results for $NO(A)$, OH^* , and NH^* with respect to the equivalence ratio and ammonia fraction. He also had quality captures of the chemiluminescence intensities of NH^*/OH^* , $OH^*/NO(A)$ and $NH^*/NO(A)$ noting that the spectral regions defined by the study as “yellow”, “red”, “blue”, “orange”, and “green” have NO_2^* and NH_2^* are the key indicator regions and excited H_2O^* is responsible for the emission in the “violet” spectral band.

It has been noted that the combustion of NH_3 under slightly rich conditions lowers NO emissions with the resultant poor combustion efficiency and significant unburnt NH_3 , hence Zhu et al. [19] investigated the combustion of premixed ammonia-hydrogen under very lean to stoichiometric conditions. They discovered that NO mole fraction exhibited monotonic relationship with OH^* suggesting that the low-cost OH^* radical can be used as an indicator for NO mole fraction for the range ($0.40 < \phi < 0.90$ and $0.25 < xNH_3 < 0.90$).

There have been several successes in the utilisation of ML techniques in predicting key features in the several engineering applications including carbon capture [20], climate change [21] and oil and gas exploration [22] etc. Following up on the success of Guiberti et al. [23] in utilising the experimental data from Zhu et al. [24] to train a Gaussian Process Regression (GPR) algorithm able to accurately predict ϕ and xNH_3 using NH^* , OH^* , CH^* and CN^* as input parameters, Mazzotta et al. [25] utilising the same algorithm predicted equivalence ratio and ammonia fraction of premixed ammonia/hydrogen/air turbulent flames using NH^*/OH^* , violet/ OH^* and NH_2^*/OH^* excited ratios across a wide range of combustion conditions. They also achieved satisfactory results by employing the same machine learning technique to estimate NO, NO_2 and N_2O emissions using NO^* , OH^* , NH^* , NH_2^* and NO_2^* as inputs. This is the first study that showcases the potential of machine learning and chemiluminescence intensities being capable of estimating key combustion features and NOx emissions in NH_3/H_2 flames.

However, it is thus evident that there is a shortage of studies in academic literature on the estimation of key combustion features and NOx using ML algorithms especially in NH_3/H_2 . It is known that the explicit representation of models allows for easy predictions and effective comparison with other models [26]. While [23] explicitly presented ϕ and xNH_3 models derived from linear regression, the better performing GPR predictions were not. Machine learning predictions done by Ballester et al. [27] using ANN also did not present their models explicitly. Tripathi et al. [28] and Mazzotta et al. [25] who utilized PLS-R in estimating ϕ of methane-air flames and GPR in predicting key combustion

characteristics and NO_x respectively had no mathematical representations of their model. Rudin [29] is of the opinion that ML models need to be explainable and interpretable and posited that interpretable models are those that are fundamentally interpretable whereas the explainable models tend to require the provision of further explanations (with tools such as heatmaps, shapely tools, sensitivity analysis, relevancy factor analysis) for the opaque models. While the models in the works of [23, 25, 27, 28] can be said to be interpretable, there was the absence of the statistics tools that aid in their explainability. In summary, the limitations of previous studies lie in the lack of explicit presentation of the models and the use of statistics tools which offer interpretability and explainability of ML models. These gaps in the reviewed works are what this study sets out to cover. The novelty of this study thus lies in its successful development of explicit models predicting ϕ , $x\text{NH}_3$ and NO_x emissions.

The other sections of this study are as follows: Section 2 describes the experimental setup, and the ML method used in developing the models, Section 3 discusses the results of the study while section 4 concludes the study with the limitations. Finally, the areas for future studies are highlighted in Section 5.

2. Methodology

This section describes the swirl burner used in the combustion, the diagnostics of the flame, the pre-processing of the data obtained, and a brief overview of the machine learning algorithm used for predictions.

2.1. Experimental setup

The tangential swirl burner used in this study is shown in Fig. 1. The experiment is carried out with the ammonia-hydrogen blend ($0.55 \leq x\text{NH}_3 \leq 0.90$), Reynold's numbers ($4000 \leq Re \leq 7000$), and equivalence ratios ($0.35 \leq \phi \leq 1.70$).

Experiments were conducted at room temperature (~ 288 K) and near atmospheric pressure (1.1 bar(a)). The flow rates for the inlet gases were prescribed by Bronkhorst flow controllers (with an accuracy better than $\pm 0.5\%$ within 15–95 % of the full scale). Reynolds numbers were varied by the adjustment of the volumetric flow rates of fuels and air. The fuel-air mixture at 288K is radially swirled before being injected into the combustion chamber (a 156 mm diameter transparent cylindrical GE214 quartz tube of height 300 mm) by means of an outer nozzle ($d = 3.15$ mm). Flame stabilisation was achieved with the use of a 22.5

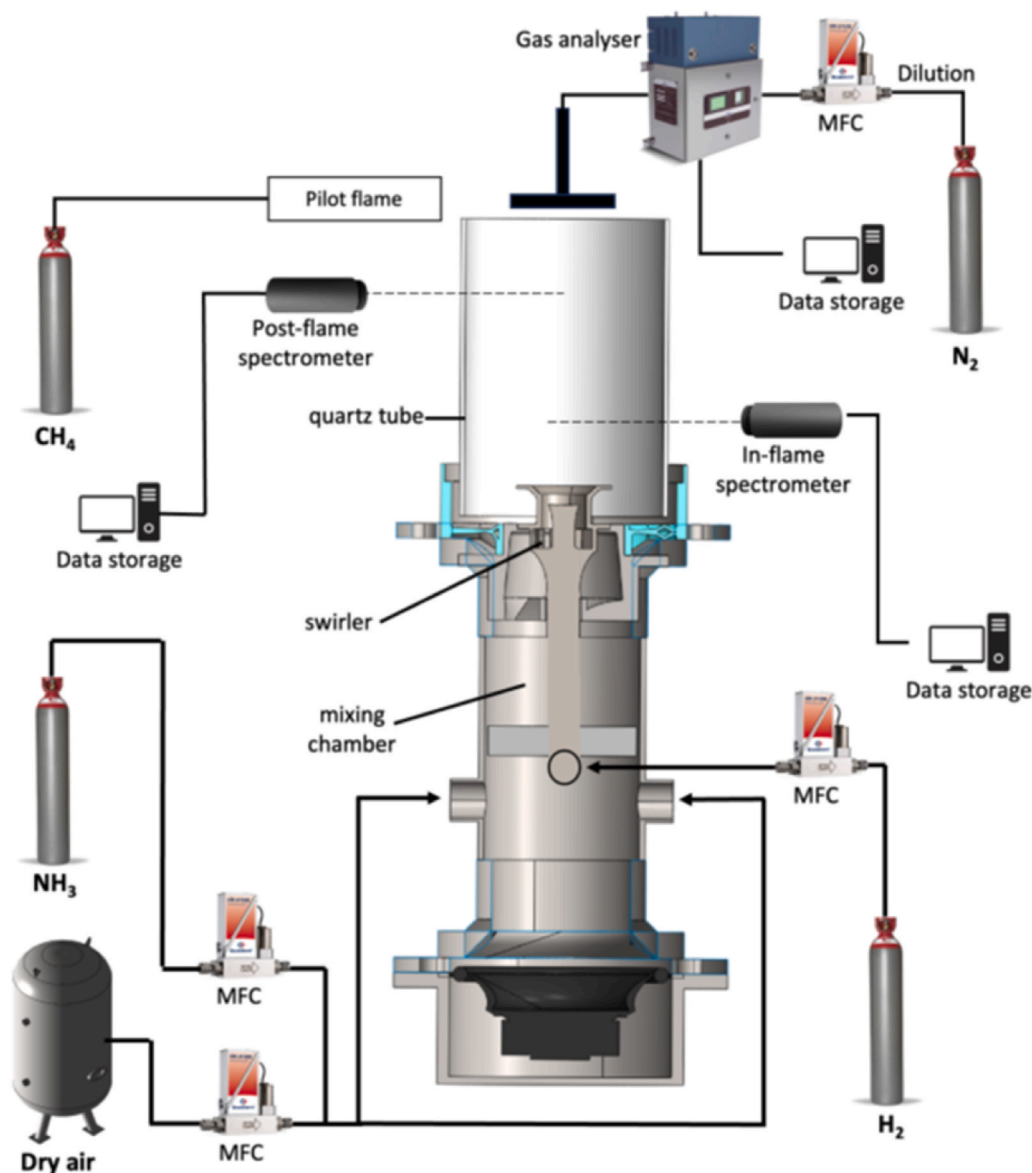


Fig. 1. Experimental setup for ammonia/hydrogen combustion.

mm diameter central bluff-body. Ignition and avoidance of extinction during blow off is achieved using a CH₄ pilot flame. The burner has a swirl number of ($S_g = 1.05$) and is calculated as shown in Equation (1).

$$S_g = \frac{A_{noz} r_{tan} \left(\frac{Q_{tan}}{Q_{tot}} \right)^2}{A_{tan} r_{noz}} \quad (1)$$

where A_{noz} represents the burner exit nozzle area, A_{tan} is the tangential inlet area, r_{tan} is the effective radius of the tangential inlet, r_{noz} represents the radius of the exit nozzle, Q_{tot} is the total flow rate and Q_{tan} depicts the tangential flow rate.

2.2. Emissions

An Emerson CT5100 quantum cascade laser analyser was used to measure the key species (NO, NO₂, N₂O, NH₃, O₂, H₂O) in the exhaust gases. It operates at 463K having a sampling frequency of 1Hz (± 1 % repeatability and 0.999 linearity). With wet readings above the range of detection of the analyser, the sample was diluted by N₂ (10 % repeatability). To depict the transient variations in emissions, data are recorded over 120 s then, a segment of the data from stable portion of the emissions was selected thus avoiding shutdown periods or transient start-ups. The arithmetic mean of each emission component was computed over the selected timeframe and then the standard deviation calculated to quantify variability of measurement and ensure data reliability.

2.3. Measuring chemiluminescence

Placed at the in-flame zone (~30 mm from burner outlet) and post-flame zone (~120 mm from burner outlet) are two different bench spectrometers (Avantes AvaSpec ULS409CL-RS-EVO) and (StellarNet Inc BLUE-Wave) respectively which simultaneously capture and record chemiluminescence. Both spectrometers are located at 150 mm from the quartz cylinder to help provide suitable signal-to noise ratio (SNR) and avoid excessive exposure to heat which interferes with optical results. The specifications of the spectrometer used for the in-flame zone capture include its sensitivity in the range of 200 nm–1100 nm and a high resolution of 0.3 nm enabling precision in the recognition of excited species and signals from the narrow bands in the spectrum. With a better resolution of 0.5 nm and sensitivity in the range of 200 nm–1150 nm, the post-flame zone spectrometer presents exhaust gas emissions from the broadband. The exposure time of the detectors is 1 s and to enhance the SNR, an average of 20 scans of images is taken to achieve convergence of the mean especially for resolution of weak signals.

Numerical integration of the chemiluminescence spectrum was utilized to generate the intensities associated with excited radicals or precise wavelength ranges of the chemiluminescence intensities. For the OH*, NH* and NH₂*, corrections were done on the background by subtracting the orange dashed line (220–350 nm) shown in Fig.A.1 (Appendix A) before integration is performed. The reader is referred to Refs. [30,31] for further information on this procedure.

2.4. Artificial neural network

Modelled on the human nervous system, Artificial Neural Network (ANN) makes use of several input signals associated with weights in what is described as simulated neurons. The ANN model multiplies the inputs and their connection weights (w), sums up the product obtained with an output produced when it passes the sum through an activation function. This output is then introduced into the next layer as an input. To vary the magnitude of this input, a bias term is added to the summation function. The significance of the activation or transfer function is to perform the non-linear transformation to the input to enable it to train itself and perform complex jobs. Fazeli et al. [32] expresses the overall relationship between the input and output data in an ANN model as

shown in Equation (2).

$$y_k = f_o \left[\sum_j w_{kj} f_h \left(\sum_i w_{ji} x_i + b_j \right) b_k \right] \quad (2)$$

where the input vector is denoted by x , connection weight from the i th neuron in input layer to hidden layer's j th neuron is represented by w_{ji} , j th hidden neuron's bias is denoted as b_j , k th output neuron's bias is denoted as b_k , the transfer functions for output and hidden neurons are represented as f_o and f_h respectively. For more information on the ANN technique, the reader is hereby referred to the works of [33,34].

2.4.1. Bayesian Regularisation algorithm

The merits of using Bayesian Regularisation Artificial Neural Network (BR-ANN) algorithm for this modelling study are numerous and include:

- (1) Offering robustness and reducing the need for cross-validation compared to conventional back-propagation networks [35].
- (2) The ability to generalize well as they are not prone to overfitting after computation and training with an effective number of variables.
- (3) MathWorks Inc. [36] which offers the neural network(NN) toolbox of the 2023 version of the software MATLAB notes that among Scaled Conjugate Gradient, Bayesian Regularisation and Levenberg-Marquardt algorithms, BR is best equipped for modelling involving small data set as that utilized in this study.

There are numerous studies that made use of the BR algorithm to model parameters e.g. estimation of solar irradiation [37] and estimation of bearing pressure on clay soil [38] etc.

2.4.2. Theory of BR

Bayesian Regularisation (BR) involves the use of a probability distribution of the network weights leading to the generation of chance estimations from the network training [39]. During the training, the performance function represented by Equation (3) is utilized to estimate the error between predicted and observed data.

$$F = E_D(D|w, M) = \frac{1}{N} \sum_{i=1}^n (\hat{t}_i - t_i)^2 \quad (3)$$

where E_D is the average sum of the squares of the errors; \hat{t}_i is the expected output; t_i is the actual output; D is the training dataset and M is the chosen topology that contains the number of layers, and the activation function used in each unit of each layer. To achieve smoother mapping in a BR network, large weights are penalized using an extra term in the objective function. An optimisation algorithm that is gradient-based is applied to ensure the minimisation of the objective function according to Equation (3) [40]. E_w represents the sum of squares of the weights.

$$F = E_D(D|w, M) + \lambda E_w(w|M) \text{ where } 0 \leq \lambda \leq 1 \quad (4)$$

Regularisation of the regression is achieved using the symbol λ known as the regularisation parameter. This helps eliminate the problem of overfitting by making the insignificant weights tend to zero and this is made possible by the introducing the inverse probability law. This law uses conditional probability to generate reverse forecasts. The hyperparameters α and β is introduced into Equation (4) to replace λ as shown in Equation (5).

$$F = \beta E_D(D|w, M) + \alpha E_w(w|M) \quad (5)$$

where $E_w(w|M)$ is $E_w = \frac{1}{n} \sum_{i=1}^n w_j^2$ are the sum of squares of the weights, α and β are estimatable hyperparameters. This term $\alpha E_w(w|M)$ is the weight decay with α as the decay rate. Suppose there is Gaussian additive noise in the targets of the acquired data, inverse probability law can

be used to revise the weight distribution to obtain Equation (6).

$$P(w|D, \alpha, \beta, M) = \frac{P(D|w, \beta, M) \cdot P(w|\alpha, M)}{P(D|\alpha, \beta, M)} \tag{6}$$

where D is the sample data used for training and the weight sharing is defined as in Equation (7).

$$P(w|\alpha, M) = \left(\frac{\alpha}{2\pi}\right)^{m/2} \exp\left\{-\frac{\alpha}{2}w'w\right\} \tag{7}$$

where w is the network weight vector, M is the neural network, P(w|α, M) represents the weights before the collection of data, m is the length of vector w, w' is the transpose of w and P(D|w, β, M) is the chance of an event happening with the network weights and is known as the likelihood function.

2.5. Source of data

In this study, the 203 data points were divided into 85 % for training set and 15 % for testing set. The adjustment of the weights of the neurons were performed by the training set while the testing data examined the performance of the network after finalization. The stopping criteria was determined by preset error indices (e.g. Mean Square Error) or when the default setting of 1000 epochs is reached.

There are 3 and 5 input parameters for combustion features (ϕ and xNH₃) and NO_x outputs, respectively. The input parameters for prediction include the radical ratios NH^{*}/OH^{*}, violet/OH^{*} and NH₂^{*}/NO₂^{*} for combustion features estimation and NO^{*}, OH^{*}, NH^{*}, NH₂^{*} and NO₂^{*} for NO_x emissions prediction. Table 1 and Table A.1 in the supplementary material shows the statistical information of the input and output variables for combustion parameters and NO_x emissions model prediction, respectively.

2.5.1. Exploratory data analysis (EDA)

This step takes place after collection of data with the aim of understanding the basic features of the data. A summary of the characteristics of the data is made and patterns identified thus uncovering embedded relationships using statistical methods. The EDA utilized in this study is the Spearman correlation heatmap which investigates the multicollinearity between the three inputs and the various outputs shown in Fig. 2a and b. The correlation coefficient (R) between the various parameters is represented by each element in the matrix. It is observed that NH₂^{*}/NO₂^{*} exhibits the strongest correlation with ϕ at a value of 0.822 and NH^{*}/OH^{*} contributes the weakest at 0.265. For the xNH₃ model, NH₂^{*}/NO₂^{*} presents the strongest correlation with ammonia fraction at an R value of 0.342 and violet/OH^{*} exhibits the weakest correlation at a value of −0.210. Based on the matrices, it can be inferred that the absence of multicollinearity is highlighted by the low coefficients among the input variables. This analysis serves as a confirmation for the use of the three input parameters for the predictions and offers a general knowledge about the contribution of each variable.

2.5.2. Data normalisation

In Machine Learning (ML), normalisation is frequently used to prepare data. This ensures that the values of all the inputs and outputs are

Table 1
Statistical dataset for equivalence ratio and ammonia fraction models.

	NH [*] /OH [*]	violet/OH [*]	NH ₂ [*] /NO ₂ [*]	ϕ	xNH ₃
Unit	a. u	a. u	a. u		
Minimum	0.0056	0.1286	0.1286	0.3000	0.5500
Maximum	2.5482	12.917	1.8170	1.7000	0.9000
Mean	0.7977	2.0349	0.8789	1.0093	0.6913
Median	0.6431	0.9589	0.7766	1.0000	0.7000
Range	2.5426	12.788	1.6327	1.3500	0.3500
Skewness	0.8418	2.1634	2.1634	0.0922	0.2208

on a similar scale. This prevents variables with larger scales from governing the training process thereby improving the accuracy of the model performance. In the dataset utilized in this study, Table 1 reveals that the data range for violet/OH^{*} is about 10 times larger than the equivalence ratio and implies that if an analysis is run on that raw data, violet/OH^{*} will falsely influence the prediction of ϕ owing to such significant difference in data values. This necessitates the normalisation of the data before use.

The data used in this work is normalised using the max-min procedure which scales the dataset to within the range −1 and 1 with its formula shown in Equation (8).

$$X_n = 2 \left(\frac{X - X_{\min}}{X_{\max} - X_{\min}} \right) - 1 \tag{8}$$

where X_n is the normalised value of a variable X, X_{min} is the minimum value of variable X and X_{max} is the maximum value of variable X.

From Table A.1, it is also evident that the raw data has widely varying ranges e.g. NO emissions is about 4000 times each of the input ranges and thus will require normalisation before being used in the BR algorithm. The normalisation formulas for each of the inputs and outputs based on Equation (8) is shown in Eq. (A.1) to Eq. (A.8) in the supplementary material.

2.5.3. Determination of the optimum model architecture

The NN architecture systematically organizes neurons into layers and defines the interconnections between these layers, as well as the activation functions and learning methods used. The feed forward multiple layer neural network which works on information movement from the input layer to the hidden layer and finally the output layer. Optimum architecture of the models of ϕ, xNH₃ and NO_x were gotten systematically. First, a small network made up of few hidden layers is tried out and then slowly increased until acceptable learning was realized. Trials with 1 neuron at a time were made in the hidden layer which accommodates a maximum of 20 neurons. To identify the optimal number of hidden layer neurons, each neuron was cloned 40 times, and the optimum number was determined to be 10. The optimal architecture is given as 3-10-1 and 5-10-1 for the combustion features and NO_x models, respectively. A 3-10-1 architecture depicts that the model uses 3 input parameters to predict 1 output processed by 10 neurons in the hidden layer of the network. The structure of the architecture for the ϕ model is shown in Fig.A.2 (Appendix A). When neurons transmit inputs, they calculate an aggregate sum of the input values and their corresponding weights, along with the bias referred to as (b1). The activation function (tanh) processes this result before it is sent to the hidden-output layer which has weights given as LW. The weighted sum of the solution from the preceding layer and the LW alongside bias b2 is estimated. Finally, this result is processed using a purelin-a linear activation function to obtain the equivalence ratio or ammonia fraction.

2.5.4. Criteria for model evaluation

Evaluating the performance of a developed ML model and ensuring constant improvements to it until the expected level of accuracy is reached is vital for the optimisation of any model. This evaluation is made possible by using statistical metrics namely coefficient of determination (R²), Mean Square Error (MSE), Root Mean Square Error (RMSE) and Average Absolute Percentage Error (AAPE). A summary of the metrics is given in Table 2. The size of the data for the modelling is given as N, the value of the experimental data is given as y_{actual}, the predictions obtained from the model is given as y_{predicted} and \bar{y} is the mean of the experimental values.

3. Results and discussion

This section discusses the results of the diagnostics of the flame and NO_x emissions from the experiments. Next, the details related to the

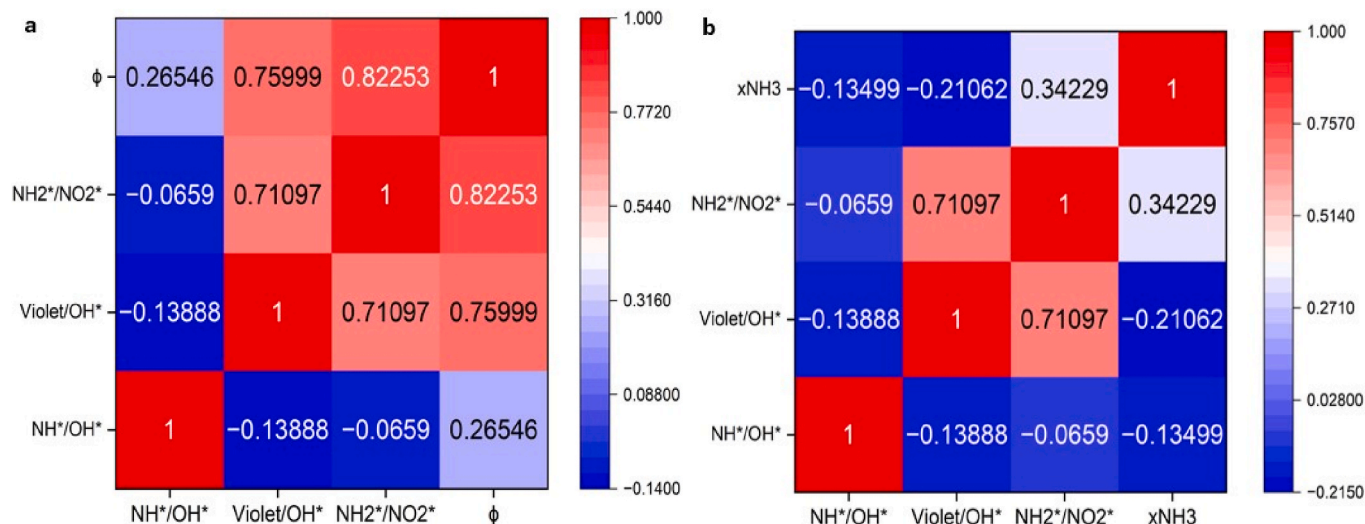


Fig. 2. Correlation matrix for (a)equivalence ratio and (b)ammonia fraction models.

Table 2
Statistical metric used in the study.

Formula	Interpretation
$R^2 = 1 - \frac{\sum_{i=1}^N (y_{\text{actual}} - y_{\text{predicted}})^2}{\sum_{i=1}^N (y_{\text{actual}} - \bar{y})^2}$	Range: 0 to 1 $R^2 = 1$ is a perfect model Range: 0 to ∞
$MSE = \frac{1}{N} \sum_{i=1}^N (y_{\text{actual}} - y_{\text{predicted}})^2$	$MSE \cong 0$ represents a good model.
$RMSE = \sqrt{\frac{1}{N} \sum_{i=1}^N (y_{\text{actual}} - y_{\text{predicted}})^2}$	Range: 0 to ∞ . $RMSE \cong 0$ represents a good model
$AAPE = \frac{100}{N} \sum_{i=1}^N \left \frac{y_i \text{ actual} - y_i \text{ predicted}}{y_i \text{ actual}} \right $	$AAPE < 10\%$ represents a highly accurate model, $AAPE$ of 10%–20% represents a good prediction, $AAPE$ of 20%–50% represents a reasonable prediction while $AAPE > 50\%$ represents an inaccurate prediction.

explicit expression of the neural network, its sensitivity analysis of input variables and performance. Finally, a comparative analysis of the working of the created models is discussed.

3.1. NOx emissions

The experimental results at constant Reynolds number of 6000 for both N_2O and NO_2 emissions show greater emissions at lean conditions and tends to decrease as x_{NH_3} increases following a similar trend in the as shown in Fig. 3a and b. NO_2 increased with decreasing ϕ and showed negligible emissions at $\phi = 1.05$ or higher. With N_2O , negligible emissions set in at $\phi = 1.1$ or higher caused by the decreased flame temperatures that are remotely induced by lower concentration of H_2 in the flame.

The NO emissions tend to increase with increasing Reynolds numbers (4000–7000) due to thermal power increase. This phenomena is confirmed by Sato et al. [41] who noted that the shape of the burner determines the fuel and air flow rates where ϕ , Re and x_{NH_3} are specified conditions. Of note is the negligible emissions at conditions of $\phi = 1.2$ and the much larger emissions at of $\phi = 0.8$. At fuel lean conditions, previous studies [42,43] have shown that the reactions $\text{NH} + \text{OH} \rightarrow \text{HNO} + \text{H}$ and $\text{NH}_2 + \text{O} \rightarrow \text{HNO} + \text{H}$ are the major sources of the HNO showing up in the main NO generation reaction $\text{HNO} + \text{H} \rightarrow \text{NO} + \text{H}_2$. The assertion that the NH and OH in the source reactions cause high NO emissions is corroborated by the fact that at lower ammonia fractions,

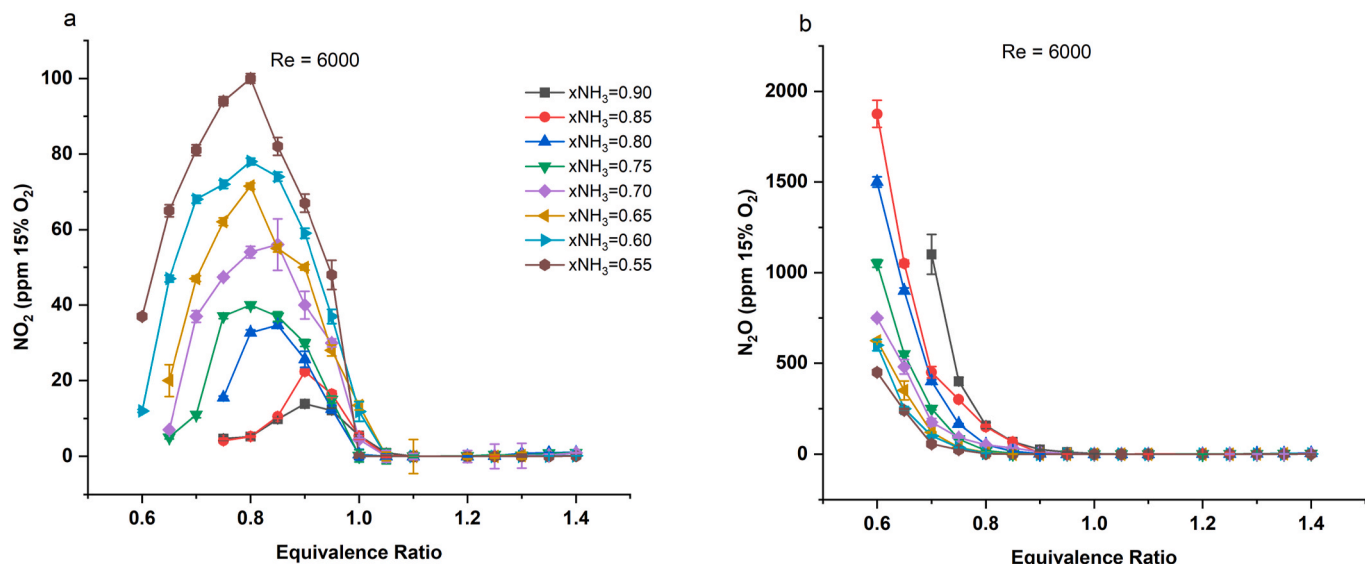


Fig. 3. Emissions of (a) NO_2 and (b) N_2O at constant Re of 6000.

OH* show stronger intensities. Results from NO emissions at different constant Re and at varying Re, show that as $x\text{NH}_3$ increases, the NO emissions decrease. As H_2 and H gotten from ammonia increases, there is a partial abundance of H_2 and H but an oxygen deficiency in the reaction. This leads to the inhibition of O and OH radical generation which directly suppresses HNO production. Studies such as [41,44] note that NO is mainly consumed by the reaction $\text{NH} + \text{NO} \rightarrow \text{N}_2\text{O} + \text{H}$. This lower NO emissions as ammonia fraction increases is evidenced by the strong presence of NH^* and NH_2^* as shown in Fig. 4.

3.1.1. Flame temperature effects

The combustion chemistry for NH_3/H_2 is highly temperature sensitive. The reaction rates are accelerated by the higher flame temperatures with the potential of aiding NOx formation. While the reaction rates may be suppressed by low flame temperatures, it could affect stability of combustion [45]. Adiabatic flame temperatures (AFT) for the combustion of NH_3/H_2 have been studied using CHEMKIN and presented in Fig. A.3 (Appendix A). It was noted that an increase in $x\text{NH}_3$ resulted in a decrease in AFT which is associated with reduced NOx emissions. Cases with varied pressures, flow rates and inlet temperatures will affect NOx formation. Localised hot spots and cooler regions in the flame zone also influence the production of emissions. Further modelling studies will look to consider these intricate variations.

3.2. Single excited radicals

The species monitored from spectral analysis come from the UV spectrum (OH^* , NO^* , NH^* , violet) and UV–visible spectrum (NO_2^* , NH_2^*). For these excited radicals, the wavelength ranges are NO^* :221.5–261.5 nm, OH^* :302–326 nm, NH^* :335–346 nm,

violet:350–400 nm, NO_2^* :400–500 nm and NH_2^* :620–645 nm and are from the in flame zone. The OH^* was the species with the maximum intensity in the UV spectrum and NH_2^* from the visible spectrum.

The trends of the measured intensities of the radicals OH^* , NH^* , NO^* and violet qualitatively match those of the measured NO and N_2O exhaust concentrations and thus can serve as useful surrogates in monitoring the performances of these noxious emissions [25]. In the visible spectrum, NH_2^* curves are bimodal and tend to increase in intensity with equivalence ratio. It is a bit complicated correlation with the emissions because of the active nature of many species for similar wavelengths. Due to its high intensity, NH_2^* plays a huge role in the consumption of NOx. These trends are similar to that obtained by Zhu et al. [17] for UV–visible chemiluminescence of laminar NH_3/H_2 flames.

It can be noticed from Fig. 5 [41] that for both $\phi = 0.8$ and $\phi = 1$ conditions, the areas of intensity of OH^* , NH^* , NH_2^* get larger with increasing Re owing to the direct variation of Re with fuel rates at a constant equivalence ratio. The flame shape depends on the volumetric gas fuel rates as it is observed that the lower the Reynolds number, the more the flame is pulled towards the burner nozzle centreline as evidenced by the behaviour of the exited OH^* and NH^* radicals. Equivalence ratio also affects the location of the flame as the spread of the flame comes with increase in production of both OH^* and NH^* at lean conditions. At rich conditions, the NH_2^* radical tends to have its centre of intensity located downstream and slightly displaced towards the sides of the burner. Signals for NH_2^* are much stronger in intensity when it is lifted and located near recirculation zones setting it up for a reaction that can lead to clean combustion. In a recent study, Viguera-Zuniga et al. [46] corroborates this assertion and notes that at rich conditions, the NH_2^* moves away from the centre of the burner and there emerges the production of NH_2 by traces of OH in the flow where there is an

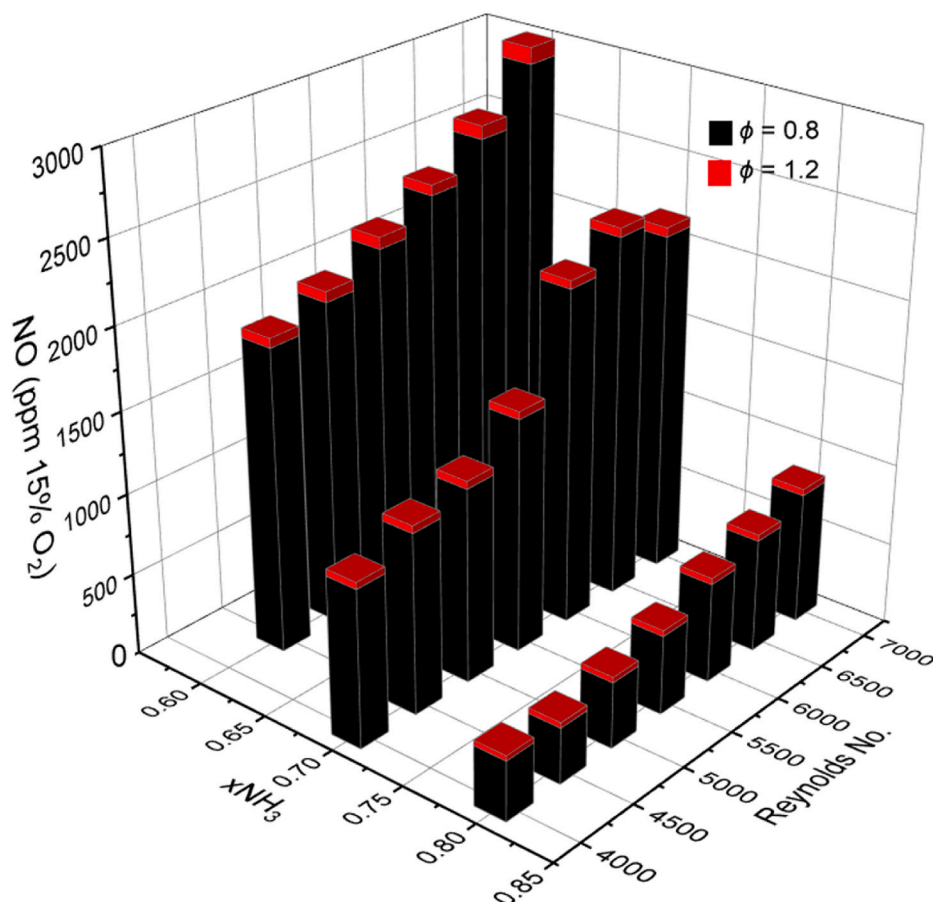


Fig. 4. NO emissions at varying Reynolds numbers and ammonia fractions measures at equivalence ratio of 0.8 and 1.2.

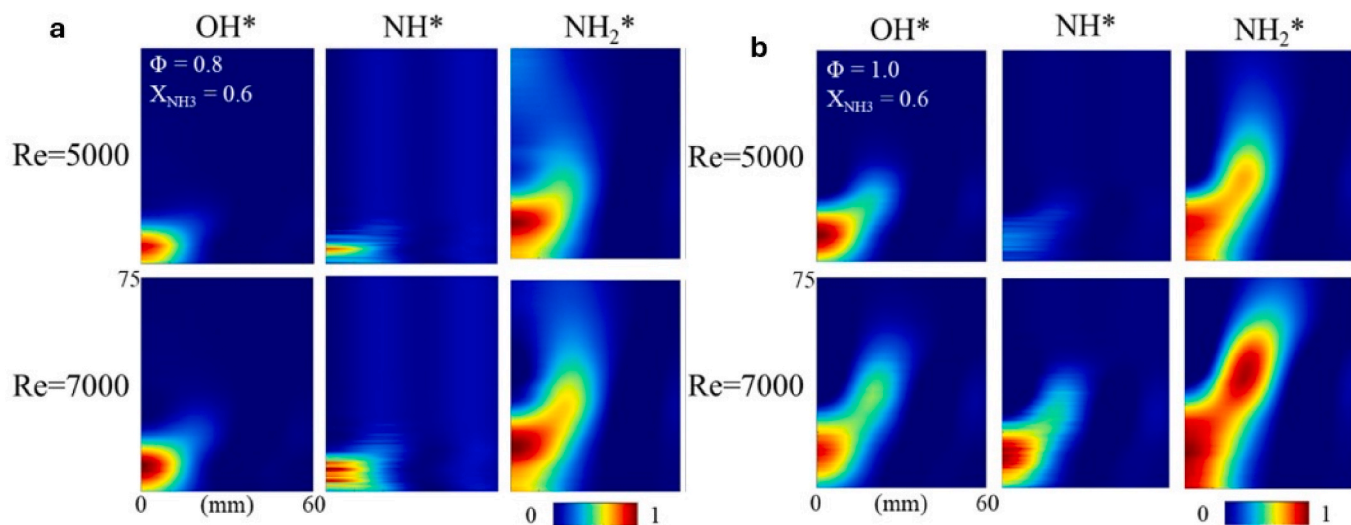


Fig. 5. OH*, NH*, NH₂* Abel transformed chemiluminescence for(a) $\phi = 0.8$ and $x_{\text{NH}_3} = 0.6$ (b) $\phi = 1$ and $x_{\text{NH}_3} = 0.6$.

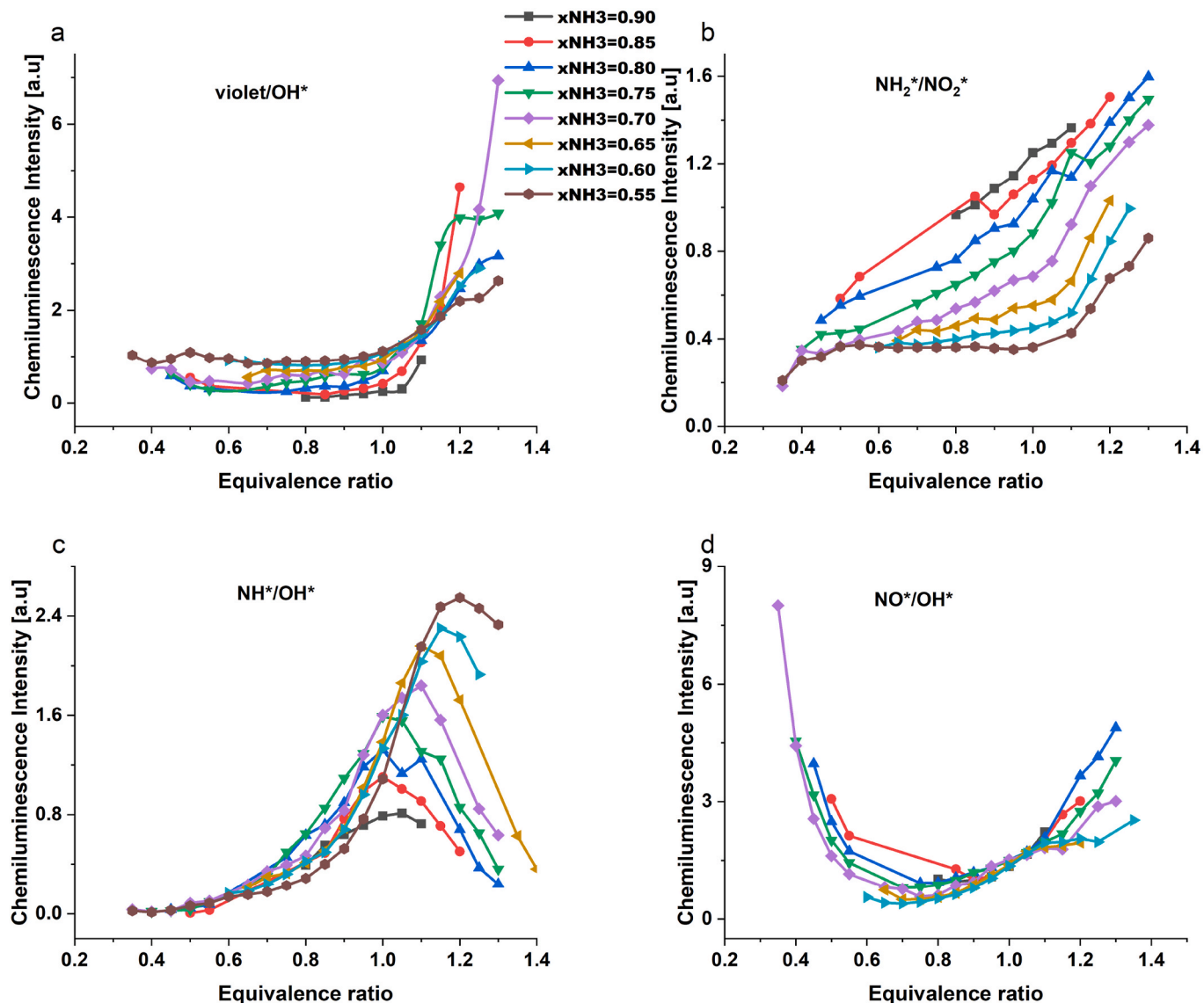


Fig. 6. Chemiluminescence intensity ratios as a function of equivalence ratios.

increased recombination with NO through the path $\text{NH}_2 + \text{NO} \rightarrow \text{N}_2 + \text{H}_2\text{O}$. To arrive at a state of NOx-less ammonia/hydrogen combustion, this reaction path needs optimisation. With the knowledge of the locations and intensities of these influential species and the help of a ML technique to assist combustion engineers in predicting the equivalence ratio and fuel fraction at which they occur, these zones that are highly concentrated with NOx - causing excited radicals can be targeted and injected with other species to ensure pollutant reduction.

3.3. Chemiluminescence intensity ratios

Turbulent flames exhibit fluctuations of intensity owing to the alteration of the flame surface area. To eliminate this phenomenon, radical intensities are studied as ratios instead of single species. To assess the potential of a ratio in sensing a flame property, its sensitivity to that particular property is critical while being insensitive to other flame properties. In this study, many intensity ratios were created from the separated spectral ranges and tested for analysis, four of the most promising ratios are presented as a function of ϕ in Fig. 6 and examined for their sensitivity or otherwise to ϕ and $x\text{NH}_3$.

NH*/OH*: This ratio increases monotonically until $\phi = 1$ with minimal sensitivity to $x\text{NH}_3$. This makes the ratio useful as a sensor for equivalence ratio in lean flames only. In richer flames, this ratio fails to sense ϕ as it varies non-monotonically with ϕ and as such it cannot be considered as a standalone surrogate for equivalence ratio.

Violet/OH*: This ratio shows a bit of promise in predicting equivalence ratio and ammonia fraction at $\phi \leq 1.1$ as it shows a very slight monotonic increase with both flame properties. At richer conditions, the ratio can serve as a good sensor for $x\text{NH}_3$.

NH₂*/NO₂*: It increases monotonically with ϕ and $x\text{NH}_3$ but it is not useful as a standalone surrogate due to its sensitivity to multiple flame features (ϕ and $x\text{NH}_3$). The trend of this ratio agrees with that observed in Ref. [17] for laminar flames and labelled as Red/Blue.

NO*/OH*: This ratio decreases non-linearly with increasing ϕ for very lean flames and then is monotonic while having a slight increase for $\phi = 0.6$ to 1.1. At higher equivalence ratios, it is slightly sensitive to $x\text{NH}_3$. This ratio cannot be used on its own to sense either ϕ or $x\text{NH}_3$.

To test the conventional ratio-based method of inferring equivalence ratio and fuel fraction, calibration curves are fitted to scatter plots of radical ratios plotted against these combustion features as shown in Fig. 7. It is evident that while a general trend developed in these plots and the 5th order polynomial curves can be used to estimate ϕ and $x\text{NH}_3$ in Fig. 7 a and b respectively, the predictions obtained from such were

poor as the regression coefficients (0.79 and 0.54) suggests. Although some excited radical ratios have capabilities that can qualify them as suitable indicators for equivalence ratio and/or ammonia fraction in case specific applications, there is however no single ratio that can accurately predict either flame property across an extensive range of operating conditions. This leads to the introduction of a machine learning technique with the ability of utilising some or all these ratios as inputs in accurately sensing these key flame features.

3.4. Mathematical representation of models

This explicit presentation of the developed models helps demystify the concept of neural network black box and thus ensure their interpretability and transparency [26]. The equations presented show how the input variables correlate with the outputs. The weights and biases are deemed the coefficients and intercepts of the BR models, respectively. The influence of the inputs on the outputs depends on the value of the weights while the biases modify the neuron's output by addition or subtraction. Table 3 shows the 40 wt and 11 biases for the ϕ model.

The ϕ model was obtained by multiplying the input variable and the corresponding sum of the weight across each row. Then the bias for each of these rows is added. The result obtained is processed by the tanh and thereafter multiplied by the LW weights producing a value for each row. For the ϕ model, these rows are 10 in number represented by a_1 to a_{10} and presented in the supplementary materials.

The sum of a_1 to a_{10} in addition to the hidden output layer bias b_2 results in the normalised ϕ model shown in Equation (9).

$$\phi_n = \sum_{i=1}^{10} a_i + 0.615 \tag{9}$$

The developed model for ϕ has been denormalised and presented in Equation (10).

$$\phi = 0.675\phi_n + 1.025 \tag{10}$$

The normalised form of the $x\text{NH}_3$ model is derived from b_1 to b_{10} in the supplementary material and presented in Equation (11).

$$x\text{NH}_{3n} = \sum_{i=1}^{10} b_i + 0.13 \tag{11}$$

The developed model for $x\text{NH}_3$ has been denormalised and presented in Equation (12)

$$x\text{NH}_3 = 0.175x\text{NH}_{3n} + 0.725 \tag{12}$$

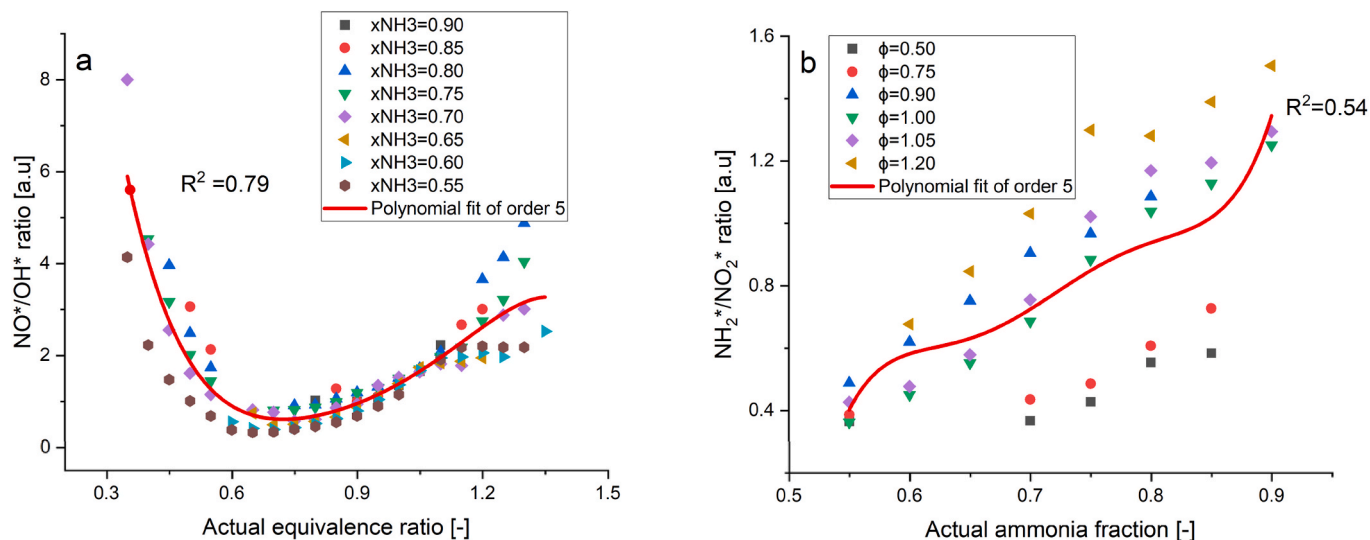


Fig. 7. Ratio-based methodology.

Table 3
Weights and biases of the equivalence ratio model.

NH*/OH*	violet/OH*	NH ₂ */NO ₂ *	b1	LW	b2
0.097633532	0.085191799	-0.023197379	-0.088905871	-0.1659588	0.615505093
-0.166863634	1.390072533	1.130772462	0.962930153	2.065010015	
0.032922488	0.021416151	-0.009198536	-0.027598124	-0.049100218	
-2.263675113	0.761226907	-0.800331271	-2.815980542	-2.028360597	
1.762451992	0.316740164	1.823018066	-0.220627015	-1.067104343	
-0.115188421	0.730027274	-1.328555594	-0.011106724	1.036647311	
-1.644046381	0.44982809	1.521253807	-3.074900209	1.737735493	
-1.279822151	0.977315117	-1.279140276	1.315958183	-2.211677473	
-0.089248918	-0.069514848	0.022607711	0.07710659	0.14398539	
0.349422531	0.0754921	1.79747877	-0.450524797	-1.294573092	

where ϕ is the equivalence ratio of the blend, ϕ_n is the normalised value of ϕ , xNH_{3n} is the normalised value of ammonia fraction, \tanh is the hyperbolic tangent, NH^*/OH^* is the radical ratio of NH^* and OH^* , $violet/OH^*$ is the radical ratio of violet and OH^* , NH_2^*/NO_2^* is the radical ratio of NH_2^* and NO_2^* . For the NOx models, all the weight and biases and their denormalization formulas have been explicitly presented in the supplementary material.

3.5. Model performance evaluation

3.5.1. Equivalence ratio and ammonia fraction models

Three metrics (R^2 , MSE, AAPE) were used in evaluating the learning performance of the models. R^2 shows the closeness of the network's prediction to that of the experimental data and thus makes the models simple and interpretable. It has a range of 0 to 1 and values closer to 1 signify that a bigger percentage of variance. ϕ model with its R^2 value of 0.9883 suggests that it can explain 98.83 % of the variance in the data. The MSE offers penalties to higher errors in the predictions. An MSE value close to zero shows the model is performing well. The effectiveness of the ϕ model is evidenced by its MSE value of 0.0047. The xNH_3 model has R^2 of 0.950 and MSE of 0.029 indicating its reasonable prediction abilities. Evaluated on their AAPE, ϕ and xNH_3 models have 3.1 % and 3.5 % errors respectively underlining their high level of accurate predictions.

The relationship between the network output variables and their targets is depicted by a regression plot. The small open circles represent the network output weights expected outputs plotted on the same graph. The ideal fit is shown by the dashed line while the solid green and blue lines stand for the best fit for test and training data, respectively. A perfect relationship between inputs and outputs is indicated by an $R = 1$ while an $R = 0$ shows a non-linear relationship between inputs and outputs. In the regression plot for the ϕ model shown in Fig. 8, with its R

value > 0.9 it can be concluded that the NN accurately estimates the equivalence ratio of the fuel blend. The regression plot for the xNH_3 model in Fig.A.4 (Appendix A) also show R values > 0.9 . It is noticed that in the regression plots a substantial percentage of the data falls on the 45° diagonal, hence the developed models can accurately predict the emissions and equivalence ratio and ammonia fraction using the radical ratios NH^*/OH^* , $violet/OH^*$ and NH_2^*/NO_2^* as input variables.

On the regression plot, the y axis is named with an equation that relates the predicted (dependent) and expected (independent) values. The target has its coefficient called the angular coefficient indicating the proportionality between dependent and independent values. This coefficient dictates optimal performance since the closer to 1 it is, the more efficient it is. An error in form of the constant in the equation is added to cause a reduction in the difference between the projected output and scaled target. For the ϕ model, the angular coefficient of both train and test datasets is 0.98 while the linear constant approaches zero (0.00014 and 0.017) for train and test datasets, respectively. In the regression plots for xNH_3 (Fig.A.4), the angular coefficients and linear constants for both training and testing show similar results to that of the ϕ model. These plots therefore reinforce the prediction capabilities of the developed models as well as the competence of the BR system.

The uniqueness of the ϕ and xNH_3 NN models is in achieving R^2 values of 0.98 and 0.95 respectively while simultaneously presenting their mathematical formulas (Equations (10) and (12)) hence their high predictive capabilities, interpretability and transparency.

3.5.1.1. Parametric importance of inputs. The influence of each input parameter on the predictions is created by analysis of regression. This can be established using several methods such as Garson's algorithm, shapley factor, relevancy factor, connection weights algorithm etc. This enhances the understanding of the 'black box' model. The relevancy factor (r) is utilized in this study to assess the effect of a particular input

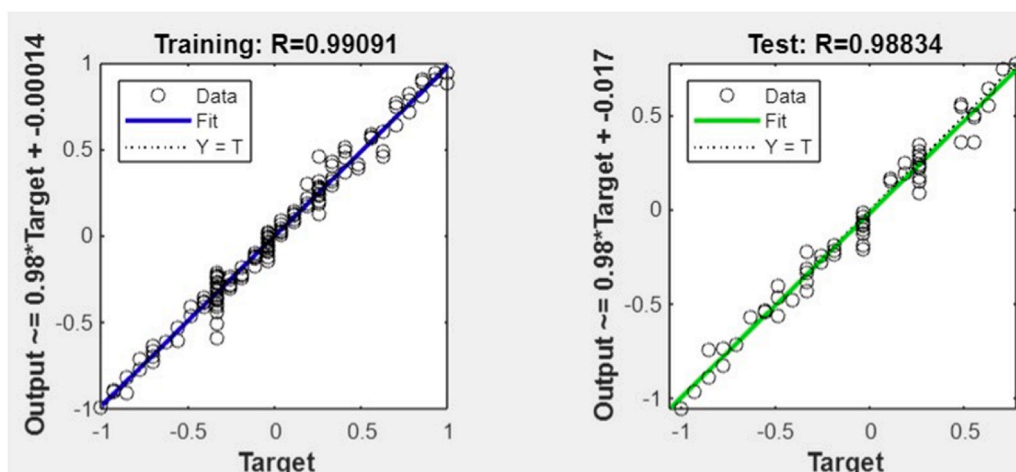


Fig. 8. Training and testing plots for the equivalence ratio model.

on the output. The method is deployed with directionality which helps in making the overall effects obvious. Equation (13) is used in the calculation of the r values of the ϕ model.

$$r(In_{p_i}, ER) = \frac{\sum_{i=1}^n (In_{p_{k,i}} - \overline{In_{p_k}})(ER_i - \overline{ER})}{\sqrt{(\sum_{i=1}^n (In_{p_{k,i}} - \overline{In_{p_k}})^2) \sum_{i=1}^n (ER_i - \overline{ER})^2}} \quad (13)$$

where $In_{p_{k,i}}$ is the i th value of the i th input parameter; $\overline{In_{p_k}}$ is the mean value of the i th input parameter, k are NH^*/OH^* , violet/ OH^* and NH_2^*/NO_2^* and ϕ ; ER_i is the i th predicted equivalence ratio and \overline{ER} is the mean predicted equivalence ratio.

From the results of the parametric importance presented in Fig. 9, it can be observed that for the equivalence ratio model, NH_2^*/NO_2^* has the highest effect ($r = 0.82$), violet/ OH^* follows closely with an r value of 0.76 while the least impact is from NH^*/OH^* with an r value of 0.26. These results are consistent with the work done by Refs. [41,47] where they noted that radical distributions have centres around the burner centreline at lower ϕ but tends to expand towards the walls of the burner as ϕ increases. They also noted that NH_2^* was more intense than OH^* and NH^* and increased with ϕ until $\phi = 1.2$ from where the reduced oxygen availability decreases its impact. This explains why the relevancy factor of NH_2^*/NO_2^* was higher than that of the other inputs in determining the ϕ . Since xNH_3 -rich zones in the flame leads to increased production of NH_2^* according to Pugh et al. [48], then NH_2^*/NO_2^* will contribute the most compared to the other input ratios in estimating ammonia fraction thus confirming the relevancy factor analysis results for the xNH_3 model.

3.5.1.2. Trend analysis. The ability of the developed models to accurately characterize the physical phenomena is the function of trend indicators. This is especially useful when the model is developed using an opaque algorithm [49]. If the predictions are expected to follow a relationship confirmed by experiments to be non-monotonic, the trend analysis will confirm if the reaction of the algorithm follows a non-monotonic form. The experimental data used was from the work of Sato et al. [41] where chemiluminescence intensity radicals OH^* , NH^* , NH_2^* and NO_x emissions were studied at varying Reynolds numbers, ammonia fractions and equivalent ratios. The equivalence ratio and ammonia fraction models were subsequently estimated and then compared to the experimental results as shown in Fig. 10. At $\phi = 1.2$, $xNH_3 = 0.6$, the maximum deviation from the experimental values was 4.1 % while at $\phi = 0.8$, $xNH_3 = 0.7$ and $\phi = 1$, $xNH_3 = 0.8$, the greatest percentage errors were 4 % and 3.2 % respectively showing that

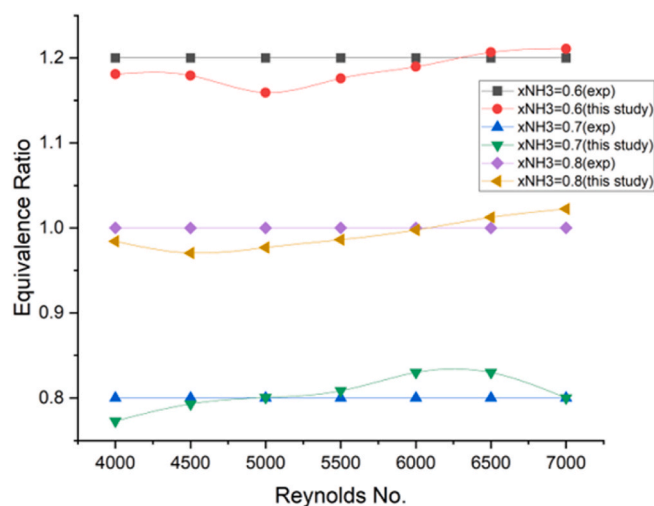


Fig. 10. Comparison of experimental and predicted equivalence ratio as a function of Reynolds number.

reasonable predictions of the equivalence ratios were obtained using the inputs of NH^*/OH^* , violet/ OH^* and NH_2^*/NO_2^* radical intensities as shown in Fig. 6.

The results from the trend analysis clearly highlights the good capabilities of the developed models to monitor emissions and thus play a huge role in the net-zero carbon economy expected in few years to come.

3.5.1.3. BR algorithm robustness to experimental errors. To account for the errors that may be existent in the experimental measurements of the excited radicals, input errors $\pm X\%$ was introduced to the NH^*/OH^* , violet/ OH^* and NH_2^*/NO_2^* ratios used for training and testing. The ideal MSE and R^2 for each introduced error was noted and the deviations from the R^2 for the prediction with no input error was represented with error bars. Fig. 11 a shows robust performance for predictions of ϕ for input errors up to $\pm 20\%$ as evidenced by the high R^2 which stay above 0.98. For errors of between $\pm 5\%$ and $\pm 10\%$, the R^2 is slightly higher than that obtained with a no input error. This phenomenon confirms the fact that ML algorithms tend to exhibit robustness to generalization when noise is introduced to the dataset [50].

Ammonia fraction predictions also showed robustness to the error in measurement because all the R^2 for the errors stayed above 0.94 (Fig. 11

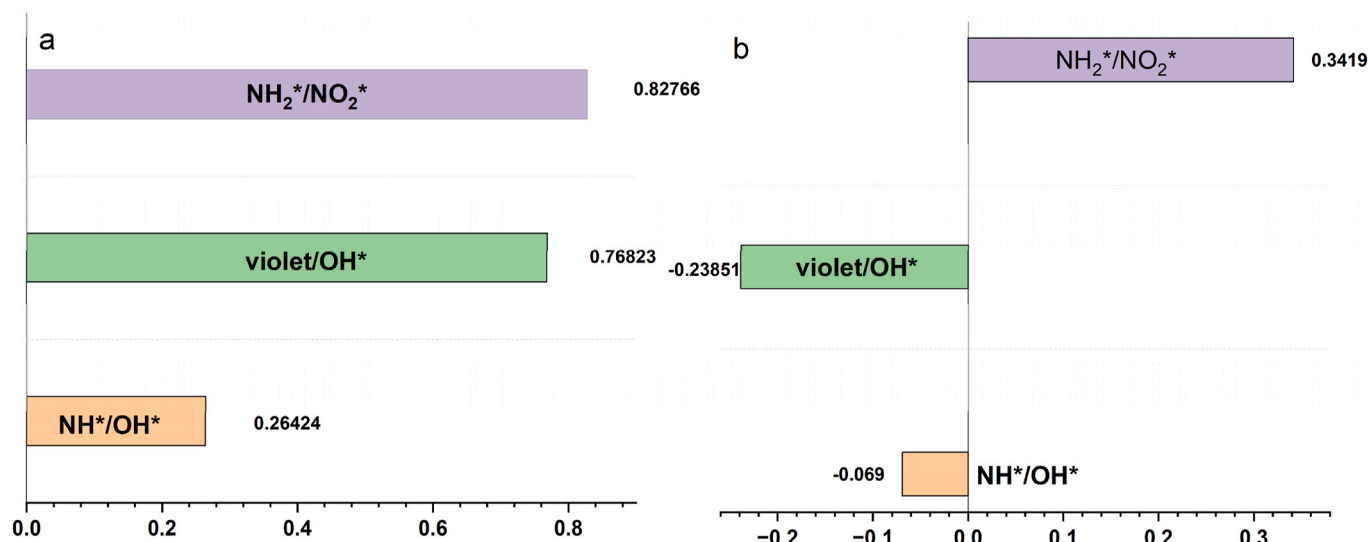


Fig. 9. Relevancy factor of input variables for (a)equivalence ratio and (b)ammonia fraction models.

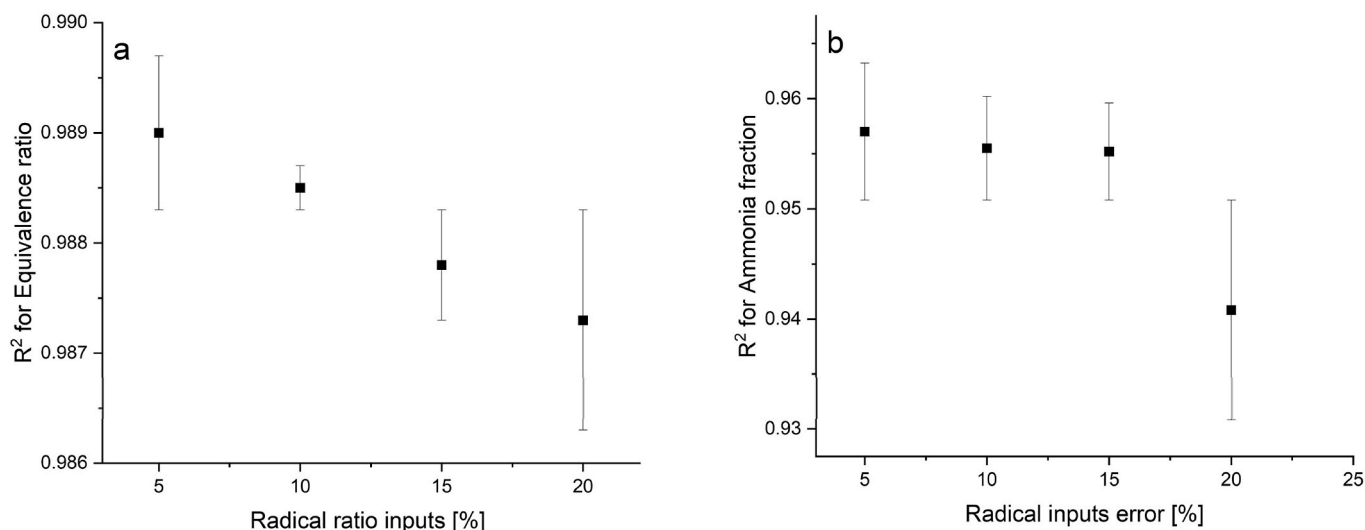


Fig. 11. Coefficient of determination for (a)equivalence ratio and (b) ammonia fraction as a function of inputs error introduced into the training and test data.

b). Between $\pm 5\%$ and $\pm 15\%$, the R^2 showed better performance than that with no input error corroborating the phenomenon noted in Ref. [50]. For ϕ and $x\text{NH}_3$ and at input error of more than $\pm 20\%$, the R^2 falls below that obtained when no input error is introduced. With this error analysis, it is evident that the BR algorithm developed in this study is robust enough to accommodate the errors obtainable in chemiluminescence intensity ratios measurements in turbulent swirl flames.

3.6. Leverage approach analysis

There exists a range of input conditions which a model can be relied on to make reasonable predictions, and the identification of these domain is essential to ensure the generalizability and accuracy of the model. Some datapoints lie outside the training range or fail to follow a well-defined pattern. These can be due to errors from measurements or some data out of the range of the model. Analysing these outliers allow the enhancement of the robustness of the model. In this study, leverage plots are used to analyse the model’s domain to detect outliers. It is seen from the leverage plot for the ϕ model in Fig. 12 that about 5 data points out of 203 data points fall outside the applicability domain $[-3$ to $3]$ which is 2.4 % of the total data points. This shows the reliability of the

model. Calculation of hat matrices H are done with Equation (14), while the standardized residuals (R_i) and the critical leverage value (H^*) and can be obtained with Equation (15) and Equation (16), respectively. The leverage plots for the models of $x\text{NH}_3$ and NO_x are shown in Fig.A.5 (Appendix A).

$$H = X(X^T X)^{-1} X^T \tag{14}$$

$$R_i = \frac{e_i}{[\text{MSE} (1 - H_i)]^{0.5}} \tag{15}$$

$$H^* = \frac{3 \times (N + 1)}{M} \tag{16}$$

where X is a 2D matrix ($M \times N$), M is the number of data points, H_i depicts the i th leverage value, R_i represents standardized residuals, N is number of input variables, T is the transpose matrix and e_i is the value of the error.

3.7. NOx predictions

Figs. 3 and 4 shows quantity of the NO_2 , NO and NO_x emissions from experiments. NO_2 achieves its peak close to $\phi = 0.85$ before gradually falling and reducing to negligible emissions at $\phi \approx 1.1$. N_2O is formed under very lean conditions. NO emissions resemble that of NO_2 qualitatively. The chemiluminescence intensities of single radicals qualitatively mirror those of the emissions discussed here, hence Bayesian Regularisation algorithm is deployed to estimate the NO_x emissions using the inputs NO^* , OH^* , NH^* , NH_2^* and NO_2^* . The comparison of the experimental data points with the predictions of NO_x from BR is shown in Fig. 13.

With the data divided into 142 for training and 61 for testing, the algorithm developed highly accurate models with R^2 values of 0.99, 0.99 and 0.97 for NO , NO_2 and N_2O , respectively. The models closely follow the NO_x emissions trend shown in Fig. 3 and Fig. 4. For the NO model, the angular coefficient of both train and test datasets is 0.98 while the linear constant approaches zero (0.01 and 0.0058) for train and test datasets, respectively. The best angular coefficient was 1 (train and test) from the N_2O model while the lowest was 0.83 (test) from the NO_2 model. The NO_x angular coefficients for both training and testing show similar results as those of the NO model. The training/testing regression and the relevancy factor analysis plots for the NO_x models are shown in Fig.A.6 and Fig.A.7 (Appendix A). The OH^* radical contributes most to the prediction of NO_x while NH_2^* has the least influence on the outputs.

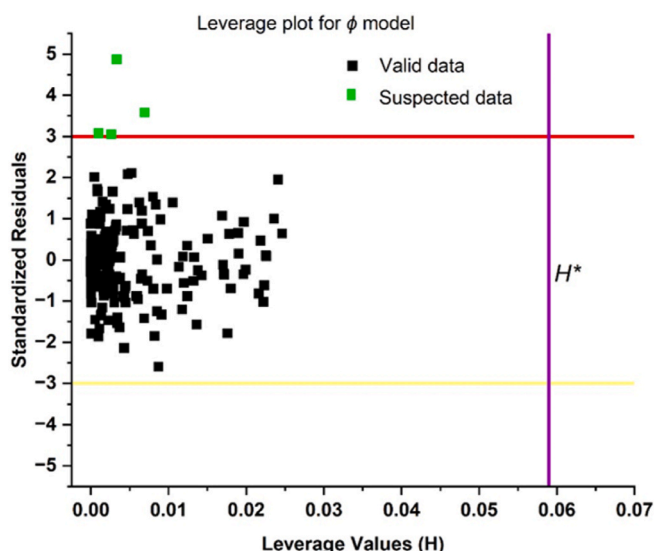


Fig. 12. Leverage plot for the equivalence ratio model.

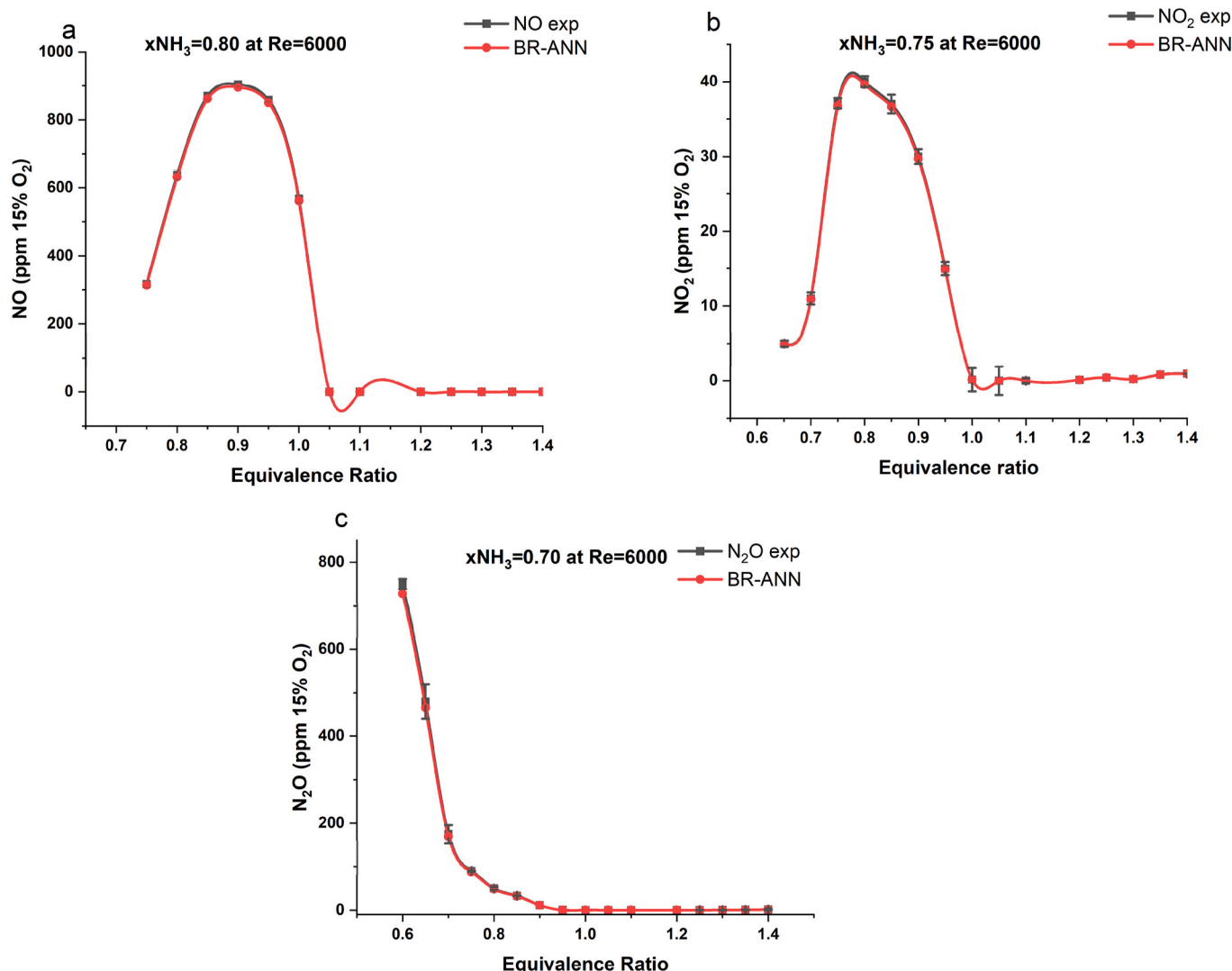


Fig. 13. Comparison of experimental (a)NO emissions at $xNH_3 = 0.80$, (b)NO₂ emissions at $xNH_3 = 0.75$ and (c)N₂O emissions at $xNH_3 = 0.70$ with their BR models.

This is corroborated by the work of [19] where it is found that OH* chemiluminescence intensities produces a monotonic relationship with the NO mole fraction for a wide range of conditions. Again OH* qualitatively mirror the emissions of NO₂ and N₂O and as such will offer profound impact on the estimation of these emissions.

These plots reinforce the prediction capabilities of the developed models as well as the competence of the BR system. These results provide a solid foundation for the development of devices that can be used to estimate and control NOx emissions. The explicit representations of the NOx models are shown in the supplementary materials as Eq. (A.10), Eq. (A.12) and Eq. (A.14) for the NO, NO₂ and N₂O models, respectively.

Comparing the predictions in this study to a similar work in [25], the BR-ANN showed better predictions for NOx and equivalence ratio as evidenced by the R² values and also presents its models explicitly. This is illustrated in Table 4.

3.8. Inference latency of the models

The duration required for a NN to make its prediction is known as the latency. This is affected by the architecture of the network, software environment and hardware platform [51]. This section will focus on calculating the inference latency of the ϕ and xNH_3 models. It is assumed that the computing device has a processing speed of 1.7 GHz

Table 4
Comparison of developed models with existing models.

Author	ML technique	Fuel blend	Coefficient of determination R ²	Model presentation
Mazzotta et al. [25]	Gaussian process	Ammonia/ Hydrogen	ϕ 0.953	Implicit
			xNH_3 0.989	
			NO 0.908	
			NO ₂ 0.954	
This study	ANN (Bayesian Regularisation)	Ammonia/ Hydrogen	N ₂ O 0.973	Explicit
			ϕ 0.98	
			xNH_3 0.95	
			NO 0.99	
			NO ₂ 0.99	
			N ₂ O 0.97	

corresponding to 1.7 billion cycles/second. Each cycle is estimated to take 755 picoseconds/cycle. Gomar et al. [52] estimates the number of clock cycles needed to process the tanh function to be 5 cycles. For ϕ and xNH_3 models, the architecture is [3-10-1] and thus requires 40 wt and 11 biases. The hidden and output layers need 50 and 5 cycles, respectively. This adds up to 55 cycles required for the activation function. Computing the total number of required cycles for a prediction gives $40 + 11 + 55 = 106$ cycles. Consequently, the inference latency is evaluated

by obtaining the product of the total cycles required and the time/cycle which gives $106 \times 755 = 80$ ns.

For the NO_x models, the architecture is [5-10-1] which thus uses 71 wt and 11 biases. The activation function requires 55 cycles and thus the total number of cycles required is $71 + 11 + 55 = 137$ cycles. The inference latency gives $137 \times 755 = 103$ ns. The models are expected to perform optimally if deployed to predict ϕ and $x\text{NH}_3$ and NO_x emissions due to its high degree of accuracy and the small amount of latency.

4. Conclusions and recommendations

In this work, chemiluminescence radicals from practical premixed NH₃/H₂ turbulent swirl flames were studied and then used to infer key flame features like ϕ , $x\text{NH}_3$ and NO_x utilising the BR artificial neural network algorithm. The following key conclusions are deduced from the findings of this study.

- i. NO emissions decrease as $x\text{NH}_3$ increases due to the reduction in OH* intensity as ammonia fraction increases. At higher $x\text{NH}_3$, the dominant species are NH* and NH₂*, prompting NO to be mainly consumed by the reaction $\text{NH} + \text{NO} \rightarrow \text{N}_2\text{O} + \text{H}$ thereby reducing NO emissions. NO₂ emissions follow a similar trend to NO. The peak emissions of NO₂ are noted to be about 40 times that of NO. All three emissions (NO, NO₂, N₂O) show negligible emissions at rich equivalence ratios.
- ii. NO emissions increase as Reynolds number increases, but this is influenced by the equivalence ratio.
- iii. The explicitly expressed and interpretable models developed in this study advances knowledge in the area of NH₃/H₂ combustion as it can be implemented as part of real-time system aimed at monitoring flames of this blend, targeting the zones of crucial emission producing species such as OH*, NH*, NH₂* etc by direct injection of other species that can reduce pollutant emissions via stopping the decay of NO_x-causing radicals.

5. Study limitations and future recommendation

- i. As much as this work serves as a solid base for subsequent development of non-invasive sensors to assist in the monitoring of turbulent swirl flames of the NH₃/H₂ fuel blend, the range of conditions taken into consideration and small amount of data employed in the development of the models constrains their use and may affect the generalisation abilities of the models.
- ii. Further research in this area will focus on developing ML models capable of estimating ϕ and $x\text{NH}_3$ for stratified and humidified flames of NH₃/H₂ at higher powers.

CRedit authorship contribution statement

Nwode Agwu: Writing – review & editing, Writing – original draft, Validation, Methodology, Data curation. **Jordan Davies:** Data curation. **Daisuke Sato:** Data curation. **Syed Mashruk:** Data curation. **Agustin Valera-Medina:** Writing – review & editing, Supervision, Resources, Funding acquisition.

Funding

The author received funding from Cardiff University for this work.

Declaration of competing interest

The authors declare that they have no known competing financial interests or personal relationships that could have appeared to influence the work reported in this paper.

Acknowledgement

The work was supported by Project AMBURN with funding from the Department for Energy Security & Net Zero (DESNZ) under award no. IFS2–06–FLO. The experimental test campaigns were conducted at the Thermofluids Laboratory (W/0.17) of Cardiff University with technical support from Mr. Malcolm Seaborne. For the purpose of open access, the author has applied a CC BY 4.0 copyright licence to any Author Accepted Manuscript version arising. Information on the data used in this publication, including access details, can be found in the Cardiff University Research Data Repository at [<https://doi.org/10.17035/cardiff.29269418>].

Appendix A. Supplementary data

Supplementary data to this article can be found online at <https://doi.org/10.1016/j.ijhydene.2025.06.062>.

References

- [1] Valera-Medina A, Xiao H, Owen-Jones M, David W, Bowen P. Ammonia for power. *Prog Energy Combust Sci* Nov 2018;69:63–102. <https://doi.org/10.1016/j.pecs.2018.07.001> (in English).
- [2] Okafor E, et al. Towards the development of an efficient low-NO_x ammonia combustor for a micro gas turbine. *Proc Combust Inst* 2019;37:4597–606. <https://doi.org/10.1016/j.proci.2018.07.083>.
- [3] MHI, mitsubishi power report breakthroughs for hydrogen combustion, ammonia burners. <https://www.powermag.com/mhi-mitsubishi-power-report-breakthrough-s-for-hydrogen-combustion-ammonia-burners/>. [Accessed 16 April 2025].
- [4] Dual-fuel ammonia for power generation in South Korea. <https://ammoniaenergy.org/topics/ammonia-hydrogen-dual-fuel/page/2/>. [Accessed 16 April 2025].
- [5] Tugboat powered by ammonia sails for the first time, showing how to cut emissions from shipping. <https://apnews.com/article/ammonia-fuel-diesel-amogy-shipping-60beccfb8894c79ddc624026fb0a8e5>. [Accessed 16 April 2025].
- [6] Ballester J, Garcia-Armingol T. Diagnostic techniques for the monitoring and control of practical flames. *Prog Energy Combust Sci* Aug 2010;36(4):375–411. <https://doi.org/10.1016/j.pecs.2009.11.005> (in English).
- [7] Gaydon W. Flames, their structure, radiation and temperature. *Appl. Mech*; 1960.
- [8] Bedard M, Fuller T, Sardeshmukh S, Anderson W. Chemiluminescence as a diagnostic in studying combustion instability in a practical combustor. *Combust Flame* 2020;213:211–25. <https://doi.org/10.1016/j.combustflame.2019.11.039>.
- [9] Soltanian H, Targhi M, Pasdarshahri H. Chemiluminescence usage in finding optimum operating range of multi-hole burners. *Energy (Calg)* 2019;180:398–404. <https://doi.org/10.1016/j.energy.2019.05.104>.
- [10] Muruganandam T, Morrell M, Nori V, Patel M, Romig B. Optical equivalence ratios sensors for gas turbine combustors. *Proceed Combust Inst* 2005;30:1601–9.
- [11] Docquier N, Candel S. Closed-loop equivalence ratio control of premixed combustors using spectrally resolved chemiluminescence measurements. *Proc Combust Inst* 2002;29:139–45.
- [12] Fowler A, Badami J. The spectrum of the hydrogen-nitrous oxide flame (in English) *P R Soc Lond a-Conta Sep* 1931;133(821):325. <https://doi.org/10.1098/rspa.1931.0151>. U19.
- [13] Wolfhard H, Parker W. A spectroscopic investigation into the structure of diffusion flames (in English) *Proc Phys Soc Lond A* 1952;65(385):2. <https://doi.org/10.1088/0370-1298/65/1/302>. &
- [14] Hayakawa A, Goto T, Mimoto R, Kudo T, Kobayashi H. NO formation/reduction mechanisms of ammonia/air premixed flames at various equivalence ratios and pressures (in English) *Mech Eng J* 2015;2(1). UNSP 14-0040210.1299/mej.14-00402.
- [15] Zhang D, Gao Q, Li B, Liu J, Tian Y, Li Z. Femtosecond laser-induced plasma spectroscopy for combustion diagnostics in premixed ammonia/air flames. *Appl Opt* Oct 1 2019;58(28):7810–6. <https://doi.org/10.1364/Ao.58.007810> (in English).
- [16] Valera-Medina A, Pugh D, Marsh P, Bulat G, Bowen P. Preliminary study on lean premixed combustion of ammonia-hydrogen for swirling gas turbine combustors. *Int J Hydrogen Energy* 2017;42(38):24495–503. <https://doi.org/10.1016/j.ijhydene.2017.08.028>.
- [17] Zhu X, Roberts W, Guiberti T. UV-visible chemiluminescence signature of laminar ammonia-hydrogen-air flames. *Proc Combust Inst* 2023;39(4):4227–35. <https://doi.org/10.1016/j.proci.2022.07.021> (in English).
- [18] Konnov A. An exploratory modelling study of chemiluminescence in ammonia-fuelled flames. Part 2 (in English) *Combust Flame* Jul 2023;253. ARTN 11278910.1016/j.combustflame.2023.112789.
- [19] Zhu X, Khateeb A, Guiberti T, Roberts W. NO and OH* emission characteristics of very-lean to stoichiometric ammonia-hydrogen-air swirl flames. *Proc Combust Inst* 2021;38(4):5155–62. <https://doi.org/10.1016/j.proci.2020.06.275> (in English).
- [20] Agwu O, et al. Carbon capture using ionic liquids: an explicit data driven model for carbon (IV) Oxide solubility estimation. *J Clean Prod* 2024;472.
- [21] Alatefi S, et al. Explainable artificial intelligence models for estimating the heat capacity of deep eutectic solvents. *Fuel* 2025;394.

- [22] Agwu O, et al. Mathematical modelling of drilling mud plastic viscosity at downhole conditions using multivariate adaptive regression splines, vol. 233; 2024.
- [23] Guiberti T, Shohdy N, Cardona S, Zhu X, Selle Land Lapeyre C. Chemiluminescence- and machine learning-based monitoring of premixed ammonia-methane-air flames. *Appl Energy Combust Sci* 2023;12//2023;16: 100212. <https://doi.org/10.1016/j.jaecs.2023.100212>.
- [24] Zhu X, Khateeb A, Roberts W, Guiberti T. Chemiluminescence signature of premixed ammonia-methane-air flames. *Combust Flame* 2021;09//2021;231: 111508. <https://doi.org/10.1016/j.combustflame.2021.111508>.
- [25] Mazzotta L, Davies J, Sato D, Borello D, Mashruk S, Valera-Medina A. Assessing the potential of a chemiluminescence and machine learning-based method for the sensing of premixed ammonia-hydrogen-air turbulent flames. *Int J Hydrogen Energy* 2025;945–54. <https://doi.org/10.1016/j.ijhydene.2024.12.262>.
- [26] Alatefi S, Alkhouh A. Explicit and explainable artificial intelligent model for prediction of CO₂ molecular diffusion coefficient in heavy crude oils and bitumen. *Results Eng* 2024. <https://doi.org/10.1016/j.rineng.2024.103328>.
- [27] Ballester J, Sanz A, Smolarz A, Barroso J, Pina A. Chemiluminescence monitoring in premixed flames of natural gas and its blends with hydrogen. *Proc Combust Inst* 2009;32:2983–91. <https://doi.org/10.1016/j.proci.2008.07.029>.
- [28] Tripathi M, Krishnan S, Srinivasan K, Yueh F. Chemiluminescence-based multivariate sensing of local equivalence ratios in premixed atmospheric methane-air flames. *Fuel* 2012. <https://doi.org/10.1016/j.fuel.2011.08.038>.
- [29] Rudin C. "Stop explaining black box machine learning models for high stakes decisions and use interpretable models instead," *Nat Mach Intell*, pp. 206–215, doi: <https://doi.org/10.1038/s42256-019-0048-x>.
- [30] Stopper U, Meier W, Sadanandan R, Stöhr M. Flow field and combustion characterization of premixed gas turbine flames by planar laser techniques. *J Eng Gas Turbines Power* 2009;131(2). <https://doi.org/10.1115/1.2969093>.
- [31] Lauer M, Sattelmayer T, Aul J. Determination of the heat release distribution in turbulent flames by a model based correction of OH* chemiluminescence. *J Eng Gas Turbines Power* 2011;133(12). <https://doi.org/10.1115/1.4004124>.
- [32] Fazeli H, Ahmadi M, Badrnezhad R, Mohammadi A. Experimental study and modeling of ultrafiltration of refinery effluents using a hybrid intelligent approach. *Energy Fuels* 2013;27(6):3523–37.
- [33] Jorjani S, Mesroghli S. Application of artificial neural networks to predict chemical desulfurization of Tabas coal. *Fuel* 2008;87(12):2727–34.
- [34] Becker K, Brenig H, Tatarczyk T. Lifetime measurements on electronically excited ch(a₂Δ) radicals. *Chem Phys Lett* 1980;71(2):242–5. [https://doi.org/10.1016/0009-2614\(80\)80156-4](https://doi.org/10.1016/0009-2614(80)80156-4) (in English).
- [35] Burden D. Bayesian regularization of neural networks. Humana Press; 2008. p. 458. https://doi.org/10.1007/978-1-60327-101-1_3.
- [36] MathWorks Inc, MATLAB update 6 (R2023b). *Natick*, Massachusetts: The MathWorks Inc; 2023. <https://www.mathworks.com>.
- [37] Molu B, Mbasso W, Naoussi S, Bajaj M, Wira P, Blazek V, Prokop S. Advancing short-term solar irradiance forecasting accuracy through a hybrid deep learning approach with Bayesian optimization. *Results Eng* 2024;23:1–16. <https://doi.org/10.1016/j.rineng.2024.102461>.
- [38] Sultana P, Dey A, Kumar D. Empirical approach for prediction of bearing pressure of spread footings on clayey soil using artificial intelligence (AI) techniques (in English) *Results Eng Sep* 2022;15. doi: ARTN 10048910.1016/j.rineng.2022.100489.
- [39] Xu M, Zeng G, Xu X, Huang G, Jiang R, Sun W. Application of Bayesian regularized BP neural network model for trend analysis, acidity and chemical composition of precipitation in North Carolina. *Water, Air, Soil Pollut May* 2006;172(1–4): 167–84. <https://doi.org/10.1007/s11270-005-9068-8> (in English).
- [40] Mackay J. *Information theory, inference and learning algorithms*. Cambridge, UK: University Press; 2008.
- [41] Sato D, Davies J, Mazzotta L, Mashruk S, Valera-Medina A, Kurose R. Effects of Reynolds number and ammonia fraction on combustion characteristics of premixed ammonia-hydrogen-air swirling flames (in English) *Proc Combust Inst* 2024;40 (1–4). doi: ARTN 10528310.1016/j.proci.2024.105283.
- [42] Mashruk S, et al. Evolution of NO production at lean combustion condition in NH₃/H₂ air premixed swirling flames (in English) *Combust Flame Oct* 2022;244. doi: ARTN 11229910.1016/j.combustflame.2022.112299.
- [43] Sun Y, et al. RANS simulations on combustion and emission characteristics of a premixed NH₃/H₂ swirling flame with reduced chemical kinetic model. *Chin J Aeronaut* 2021;34(12):17–27. <https://doi.org/10.1016/j.cja.2020.11.017>.
- [44] Kim J, Song J, Ku J, Kim Y. Combustion characteristics of premixed ammonia-hydrogen/air flames in a swirl model combustor. *Int J Hydrogen Energy* 2023: 360–3199.
- [45] Okumura Y, Kikuchi K, Yagawa N, Matsunmai T. Premixed combustion characteristics of offgas during ammonia cracking process, vol. 381; 2025.
- [46] Viguera-Zuniga M TdCM, Davies J, Mashruk S, Valera-Medina A. Analysis of excited species formation across the flame of various ammonia-hydrogen fired combustor geometries. *Energy Technol* 2024. <https://doi.org/10.1002/ente.202401404>.
- [47] Mashruk S, Brequigny P, Mounaim-Rousselle C, Valera-Medina A. Combustion performances of premixed ammonia/hydrogen/air laminar and swirling flames for a wide range of equivalence ratios. *Int J Hydrogen Energy* 2022;47:41170–82. <https://doi.org/10.1016/j.ijhydene.2022.09.165>.
- [48] Pugh D, et al. An investigation of ammonia primary flame combustor concepts for emissions reduction with OH*, NH* and NH* chemiluminescence at elevated conditions. *Proc Combust Inst* 2021;38(4):6451–9. <https://doi.org/10.1016/j.proci.2020.06.310> (in English).
- [49] Baucells M, Plischke E, Barr J, Rabitz H. Trend analysis in the age of machine learning. Working Paper; 2021, 3867894. <https://doi.org/10.2139/ssrn.3867894>.
- [50] Sietsma J, Dow R. Creating artificial neural networks that generalize. *Neural Netw* 1991;4(1):67–79. [https://doi.org/10.1016/0893-6080\(91\)90033-2](https://doi.org/10.1016/0893-6080(91)90033-2) (in English).
- [51] Mendoza D, Wang S. Predicting latency of neural network inference. Report submitted to Stanford University; 2020. p. 6. https://cs230.stanford.edu/projects_fall2020/reports/55793069.pdf.
- [52] Gomar S, Mirhassani M, Ahmadi M. Precise digital implementations of hyperbolic tanh and sigmoid function (in English). In: *Conf rec asilomar C*; 2016. p. 1586–9 [Online]. Available: <Go to ISI>://WOS:000406057400279.